JOURNAL OF PROPULSION AND POWER
Vol. 22, No. 3, May–June 2006

Turbulence Modeling Effects on Calculation of Lobed Nozzle Flowfields

Nicholas J. Georgiadis*
NASA John H. Glenn Research Center at Lewis Field, Cleveland, Ohio 44135
Christopher L. Rumsey†
NASA Langley Research Center, Hampton, Virginia 23681
and
Dennis A. Yoder‡ and Khairul B. M. Q. Zaman§
NASA John H. Glenn Research Center at Lewis Field, Cleveland, Ohio 44135

Two Reynolds-averaged Navier–Stokes solvers, CFL3D and WIND, are applied to the subsonic turbulent jet flowfield originating from a six-lobed nozzle, with emphasis placed on turbulence modeling effects. The turbulence models investigated include linear one-equation and two-equation models and nonlinear two-equation explicit algebraic stress model (EASM) formulations. Two nozzle operating points are investigated, corresponding to exit Mach numbers of 0.30 and 0.94. Comparisons of calculated mean axial velocities and turbulence intensities are made with experimental data. All of the turbulence models were deficient in predicting the initial mixing rate exhibited by the experimental data. The one-equation model provided the best agreement with experimental data in the near field of the jet. The linear two-equation models and a modified EASM provided better agreement with data in the farfield. The Mach 0.30 k–ω EASM calculation required a time-accurate calculation because of significant unsteadiness in the initial jet region, which is believed to be characteristic of the nozzle flow under consideration.

Nomenclature

D	=	equivalent jet diameter
k	=	turbulent kinetic energy
$\mathcal{P}$	=	turbulent production
P_T	=	stagnation pressure
P_∞	=	ambient static pressure
S_{ij}	=	rate of strain tensor
t	=	time
U_{jet}	=	jet-exit velocity
u	=	velocity
u'	=	fluctuating velocity
W_{ij}	=	vorticity tensor
x, y, z	=	Cartesian coordinates
y^+	=	wall-normal coordinate
ϵ	=	turbulent dissipation rate
κ	=	von Kármán constant
ν	=	kinematic viscosity
ν_t	=	kinematic eddy viscosity
ρ	=	density
τ	=	turbulent timescale
τ_{ij}	=	turbulent stress tensor
ω	=	specific turbulent dissipation rate

I. Introduction

COMPUTATIONAL-FLUID-DYNAMICS codes have become an attractive option for the analysis of aerospace systems as a result of advances in flow solver and computer hardware technologies. For the investigation of one particular class of flows, that of aircraft engine exhaust nozzles, Reynolds-averaged Navier–Stokes (RANS) solvers have been used extensively in recent years. In the RANS approach, all effects of turbulence are replaced with a turbulence model. However, with realistic nozzle flows typically dominated by turbulent mixing, the accuracy of a flow simulation is usually determined by the capabilities of the turbulence model employed. Previous studies, such as those of Barber et al.[1] and Georgiadis et al.[2] investigated linear two-equation turbulence models for calculation of benchmark nozzle and mixing-layer test cases, and determined that such models have difficulty predicting the effects of compressibility, high temperatures, and three-dimensional flow features.

In recent years, nonlinear explicit algebraic-stress model (EASM) formulations have been explored for improving the capability to predict the aerodynamics and aeroacoustics of turbulent jets.[3–6] To date, these studies have indicated that EASM approaches have difficulties similar to linear two-equation models in underpredicting initial jet mixing rates. However, it has been noted that calibrations of key EASM coefficients have not been extensively performed for free shear-layer flows. EASM approaches have potential over linear two-equation models to be more accurately applied to flows with significant turbulent anisotropy.

To address the complexities of three-dimensional nozzle flowfield development, a nozzle having a six-lobed configuration is investigated in the current work. Although this nozzle is more geometrically complex than those investigated in the studies of Refs. 1 and 2, the nozzle was tested using unheated air and had a subsonic exit condition. As a result, temperature and compressibility effects are not significant factors, and the effects of three-dimensional flow could be isolated. Two general-purpose RANS solvers, CFL3D and WIND, are used to obtain calculations for this lobed nozzle configuration. Linear one- and two-equation turbulence models, such as those employed in Refs. 1 and 2, are used here. In addition, EASM formulations are also investigated.

II. Experimental Configuration

In the experiments of Zaman et al.,[7] the freejets developing from a circular nozzle and three-lobed nozzles, having 6, 10, and 14

Presented as Paper 2003-1271 at the AIAA 41st Aerospace Sciences Meeting and Exhibit, Reno, NV, 6–9 January 2003; received 14 April 2005; revision received 14 November 2005; accepted for publication 21 November 2005.

*Aerospace Engineer, Nozzle Branch. Associate Fellow AIAA.
†Aerospace Engineer, Computational Modeling and Simulation Branch. Associate Fellow AIAA.
‡Aerospace Engineer, Nozzle Branch. Senior Member AIAA.
§Aerospace Engineer, Nozzle Branch. Associate Fellow AIAA.

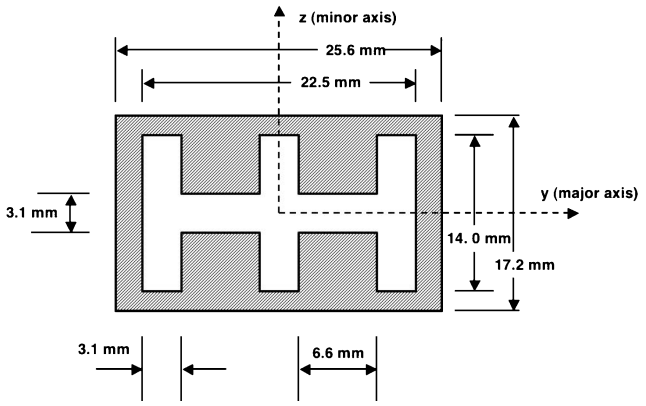

Fig. 1 Schematic of nozzle exit for six-lobed configuration.

lobes, respectively, were investigated. These lobed nozzle configurations exhibited lower turbulence intensities and lower far-field noise than nonlobed configurations. The six-lobed configuration, shown schematically in Fig. 1, is under investigation in the current work. All of the nozzles investigated in Ref. 7 had convergent interiors with a 0.25-in. (6.4-mm)-long constant-area cross section just upstream of the nozzle-exit plane, which produces a jet with initially only an axial-velocity component. Forced mixers, such as those using convoluted surfaces at the entrance of a nozzle mixing section, produce jets having extensive streamwise vortices and three dimensionality, as discussed in Ref. 8. Although the nozzle considered here is not a forced mixer, significant three-dimensional flow structures do develop as the lobed nozzle flows mixes with the ambient air.

The equivalent diameter D, based on an area-equivalent round nozzle, was 0.58 in. (14.7 mm) for all of the nozzles. In the experiments, hot-wire anemometry was used to make measurements of mean flow axial velocity and turbulence intensity fields for Mach 0.30 and Mach 0.94 nozzle-exit operating points. It is discussed in Ref. 7 that using the hot-wire technique in high-speed flows, as in the case of the Mach 0.94 nozzle flow considered here, has limitations. As a result, measurements were only taken along the jet centerline for the Mach 0.94 case. For the Mach 0.30 case, measurements were not only made along the centerline, but also detailed velocity and turbulence intensity profiles were obtained along the jet major and minor axes at several axial stations.

III. Computational Modeling

Two widely used RANS solvers, WIND[9] and CFL3D,[10] are employed to conduct the computational investigations of the six-lobed nozzle in this work. Both WIND and CFL3D are structured-grid finite volume codes using upwind numerical schemes for most flow applications, and in the current study the flux-difference-splitting technique of Roe was employed to calculate fluxes at cell faces. Both WIND and CFL3D can accommodate point-matched, patched, or overset grids for complex computational domains and can employ local time-step scaling and grid sequencing to accelerate convergence for steady-state problems. CFL3D also has a multigrid capability for convergence acceleration. Grid sequencing in both WIND and CFL3D was used for the calculations obtained in the current study.

A. Turbulence Modeling

Both CFL3D and WIND have a broad set of turbulence models available, all of which fall into the class of eddy-viscosity formulations. In the current study, a subset of these models was chosen to investigate the effects of model formulations and sophistication, that is, linear one-equation, linear two-equation, and nonlinear two-equation EASM approaches. In the cases of the same model from this subset being available in both CFL3D and WIND, solutions with both codes were obtained to isolate any differences as a result of code numerics.

The linear one-equation model investigated with both solvers is the Spalart–Allmaras[11,12] (SA) formulation. The SA model is available in both CFL3D and WIND. The linear two-equation turbulence models investigated here are the Chien k–ϵ[13] model and the shear-stress transport (SST) model of Menter.[14,15] The SST model employs a k–ω formulation in the inner region of wall boundary layers and switches to a transformed k–ϵ formulation in the outer region of boundary layers and in free shear-layer/mixing regions. The Chien k–ϵ model is available in WIND, and the SST model is available in both CFL3D and WIND.

Significant work in recent years to implement nonlinear EASM formulations in the CFL3D code has resulted in two models that are currently available. The first EASM is derived in a k–ϵ form,[16,17] and the second is derived in a k–ω form.[17] Unlike linear two-equation models, EASM formulations are sensitive to turbulent stress anisotropies and have a direct relation to the full Reynolds-stress model. As a result, EASM models have the capability to include more relevant flow physics than the linear models. However, they are also solved using a two-equation approach, and as a result are not significantly more computationally expensive than linear two-equation models. The k–ω EASM formulation available in CFL3D was used in the current study. The k–ϵ EASM model of Rumsey et al.[16] and Rumsey and Gatski[17] has recently been installed in WIND, as detailed in Ref. 6, and was also investigated in this study.

During the course of the current nozzle calculations, two coefficients controlling the diffusion terms in the underlying two-equation model of the k–ω EASM installed in CFL3D were modified. As a result, the principal equations defining this model are provided in the following discussion. The turbulent stress tensor of the EASM (for both k–ϵ and k–ω) is

$$\tau_{ij} = \tfrac{2}{3}k\delta_{ij} - 2\nu_t^*\left\{S_{ij} - \tfrac{1}{3}S_{kk}\delta_{ij} + \left[a_2a_4(S_{ik}W_{kj} - W_{ik}S_{kj}) - 2a_3a_4\left(S_{ik}S_{kj} - \tfrac{1}{3}S_{kl}S_{lk}\delta_{ij}\right)\right]\right\} \tag{1}$$

where S_{ij} is

$$S_{ij} = \frac{1}{2}\left(\frac{\partial u_i}{\partial x_j} + \frac{\partial u_j}{\partial x_i}\right) \tag{2}$$

and W_{ij} is

$$W_{ij} = \frac{1}{2}\left(\frac{\partial u_i}{\partial x_j} - \frac{\partial u_j}{\partial x_i}\right) \tag{3}$$

The kinematic eddy viscosity ν_t^* is

$$\nu_t^* = C_\mu^* k\tau = -k\alpha_1 \tag{4}$$

where the turbulent timescale is $\tau = 1/\omega = k/\epsilon$. The quantity α_1/τ is equivalent to $-C_\mu^*$ and is obtained from the solution to a cubic equation at every point in the flowfield. The solution procedure is described in detail in Ref. 17.

The form of the k–ω model used in CFL3D as the underlying two-equation model for the EASM is

$$\frac{\mathrm{D}k}{\mathrm{D}t} = \mathcal{P} - f_{\beta^*}k\omega + \frac{\partial}{\partial x_k}\left[\left(\nu + \frac{\nu_t^*}{\sigma_k}\right)\frac{\partial k}{\partial x_k}\right] \tag{5}$$

$$\frac{\mathrm{D}\omega}{\mathrm{D}t} = \gamma\frac{\omega}{k}\mathcal{P} - \beta\omega^2 + \frac{\partial}{\partial x_k}\left[\left(\nu + \frac{\nu_t^*}{\sigma_\omega}\right)\frac{\partial \omega}{\partial x_k}\right] \tag{6}$$

where the production of k is given by

$$\mathcal{P} = -\tau_{ij}\frac{\partial u_i}{\partial x_j} \approx 2\nu_t^* S_{ij}S_{ij} \tag{7}$$

The form of the function f_{β^*} is given in Ref. 17. The two coefficients in the k–ω EASM that were modified are σ_k and γ. In the original model, $\sigma_k = 2$, and $\gamma = 0.575$. The modified coefficients are $\sigma_k = 1$ and $\gamma = 0.53$. The motivation for this change was that in

the original model the dissipation was too low near boundary-layer and shear-layer edges, which frequently resulted in abrupt slope changes in predicted mean-flow quantities. The problem was particularly evident for jet flows, as shown in Ref. 18. In addition, the rate of jet mixing was found to be too low relative to experimental measurements. Reducing σ_k improved results near the edge of the jet considerably. It also improved the slope characteristics near the edge of boundary layers. In Ref. 19, a similar change to σ_k in a linear k–ϵ model (σ_k changed from 1.36 to 1.0) also resulted in greater mixing and better agreement with experimental observations.

The γ coefficient multiplies the production term in the ω equation, and it also affects the value of σ_ω, through the equation

$$\sigma_\omega = \kappa^2 \Big/ \left[\sqrt{c_\mu}(\beta - \gamma)\right] \tag{8}$$

where $\kappa = 0.41$, $\beta = 0.83$, and $c_\mu = 0.0895$.

Use of Eq. (8) insures correct log-layer characteristics. In the original model, $\gamma = 0.575$ results in $\sigma_\omega = 2.2035$. In the revised model, $\gamma = 0.53$ corresponds to $\sigma_\omega = 1.8730$.

The k–ω EASM with the modified coefficients was subsequently tested for a variety of validation aerodynamic flowfields, including flat plate, backstep, transonic diffuser, axisymmetric bump, airfoils, wing, ejector nozzle, and curved duct. These tests were generally very successful and were documented in Ref. 18. Because of the general success with the modified coefficients, both for the current nozzle case as well as for the validation flows, the default k–ω EASM model in CFL3D was permanently changed, incorporating the modified coefficients. The original and new sets of coefficients are compared in the current study for the Mach 0.94 nozzle case, as will be addressed in the Results section.

B. Computational Grid and Boundary Conditions

A computational grid having approximately 2.57 million points distributed across six zones was constructed as follows. Because of horizontal and vertical symmetry of the nozzle configuration, shown in Fig. 1, one quadrant of the nozzle was modeled, which is sufficient using the RANS approaches considered here. Examining Fig. 1, the x–y plane of symmetry will be referred to as the major axis, while the x–z plane of symmetry is the minor axis. Figure 2 provides a perspective view of the grid along these two symmetry planes. The nozzle geometry representing the internal flow region upstream of the nozzle-exit plane shown in Fig. 1 was represented by three zones with point-to-point matching between zones. The grid was packed to the nozzle wall surfaces such that the average $y+$ of the first point off any wall did not exceed 2.5.

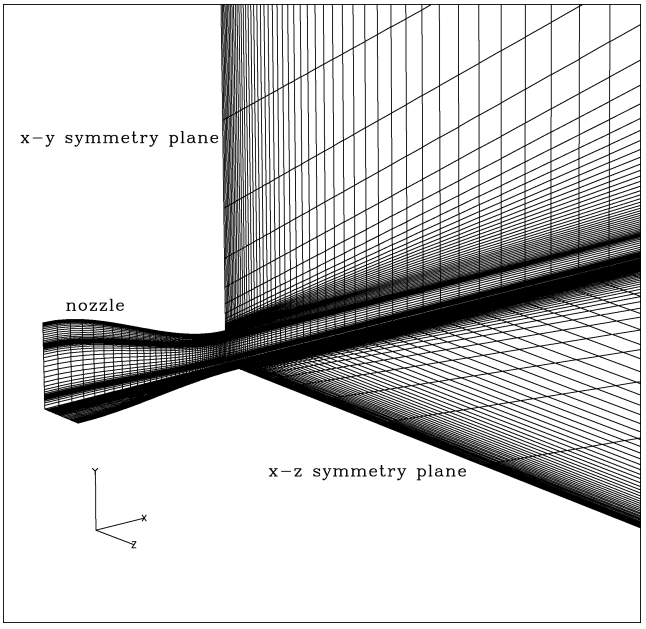

Fig. 2 Perspective view of grid along symmetry planes (every other point shown for clarity).

The inflow boundaries of the three zones representing the internal nozzle geometry specified the nozzle stagnation pressure, which corresponds to the ideally expanded Mach number of the two cases investigated in this study: $P_T/P_\infty = 1.0644$ for Mach number 0.30 and $P_T/P_\infty = 1.7675$ for Mach number 0.94. The stagnation temperature was set to the ambient static temperature because the experiments of Zaman et al. used unheated laboratory air in the nozzle supply lines. Two grid zones were used to represent the ambient air surrounding the nozzle configuration upstream of the nozzle-exit plane. The inflows of these two blocks set the inflow stagnation temperature and pressures equal to the ambient static values such that a quiescent ambient condition could be modeled, as existed in the experiment. Far-field boundaries surrounding the jet were set as inviscid walls. All nozzle surfaces, including the base regions, were modeled as adiabatic no-slip surfaces. The three nozzle zones and two ambient inflow zones interfaced with one downstream zone in which the exiting jet flow mixed with the ambient air. The downstream static pressure was set to the ambient pressure.

C. Turbulence Intensity Calculation

Mean axial velocities and turbulence intensities from the solutions are compared with the experimental data of Zaman et al.[7] The axial turbulence intensities were obtained from $\tau_{11} = \overline{u'u'}$ and employing the appropriate turbulent stress expression for each model as follows. From the EASM solutions, the turbulent stress tensor given by Eq. (1) was used. For the linear one-equation and two-equation model solutions, the Boussinesq approximation was employed:

$$\tau_{ij} = \tfrac{2}{3}k\delta_{ij} - 2\nu_t\left(S_{ij} - \tfrac{1}{3}S_{kk}\delta_{ij}\right) \tag{9}$$

Although the two-equation models directly provide the turbulent kinetic energy k used in Eq. (9), this quantity must be approximated for the one-equation Spalart–Allmaras model. In Ref. 12, this approximation for k is given by

$$k = \nu_t\sqrt{2S_{ij}S_{ij}}\Big/2a_1 \tag{10}$$

where $a_1 = 0.155$ is the structure parameter.

IV. Results

In this section, results for the Mach 0.30 case, for which there are more extensive experimental data available, are presented first, followed by the Mach 0.94 case results. For each of these two cases, comparisons of CFL3D and WIND results are made within each class of turbulence model, that is, linear one-equation, linear two-equation, and EASM to isolate any differences from one code to the other when using a similar turbulence model. Then, to highlight differences caused by turbulence model, separate results from CFL3D and WIND are presented, for all of the turbulence models used for each code.

A. Mach 0.30 Nozzle Flow

To determine if the computational grid were sufficient for modeling the dominant flow characteristics of the nozzle flows under consideration, a comparison of intermediate solutions obtained with every other point in each computational direction (termed half-grid in the subsequent discussion) was made with solutions obtained using the full grid. Figure 3 provides a comparison of axial velocity and turbulence intensity profiles along the major axis obtained from CFL3D calculations with the SST model using the half-grid and full grid. Although a complete grid-sensitivity study would investigate a third computational grid with even more points than that in the current full grid (2.57 million points), the results shown in Fig. 3, with only minor differences between the two solutions, indicate that the full grid is sufficient. Comparisons of solutions for the other turbulence models obtained with the two grids indicated similar agreement as those shown here for the SST results.

A comparison of centerline axial velocities obtained within each class of turbulence model is presented in Fig. 4. For the two models

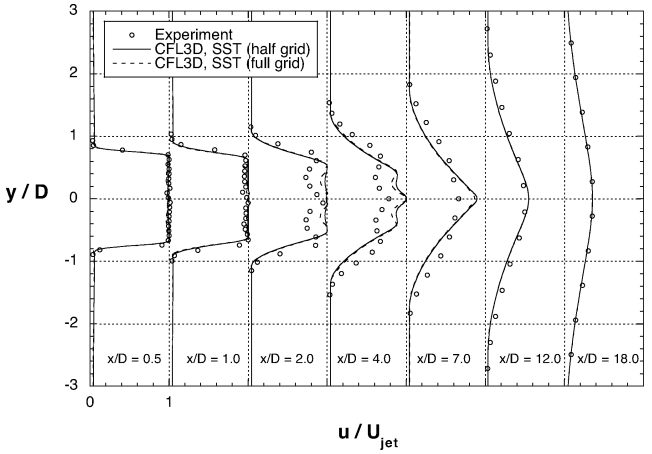

a) Mean velocities along major axis

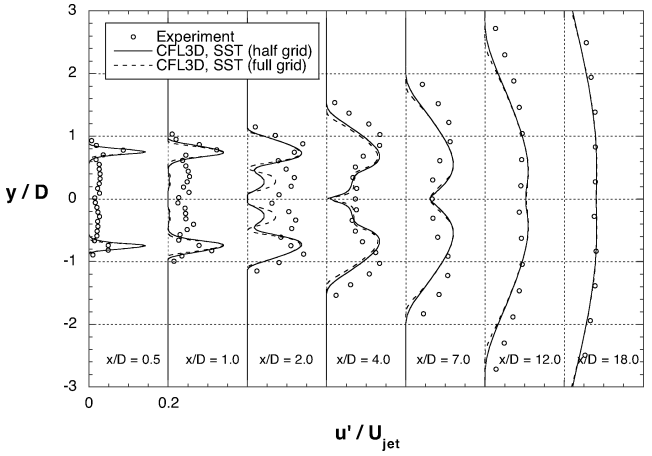

b) Turbulence intensities along major axis

Fig. 3 Grid-sensitivity effects using CFL3D, SST turbulence model.

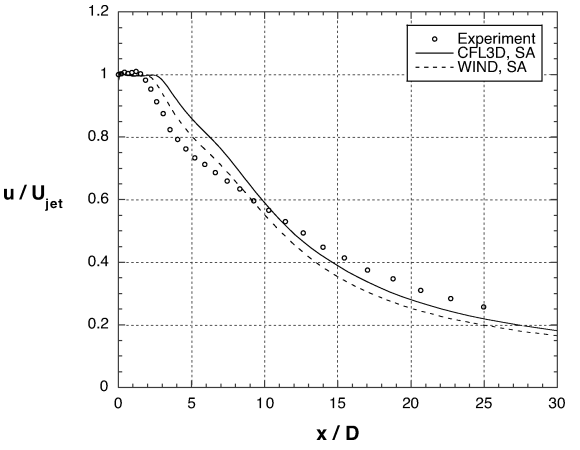

a) One-equation models

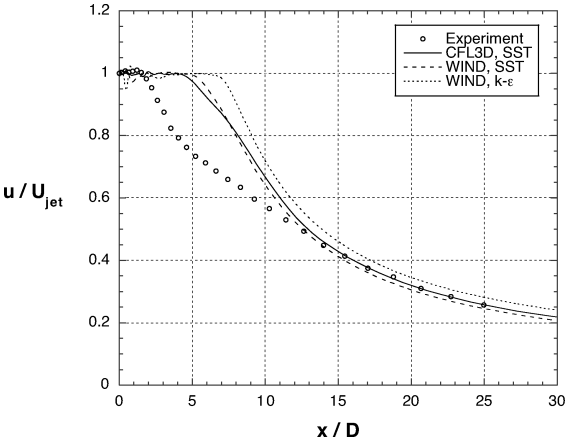

b) Two-equation models

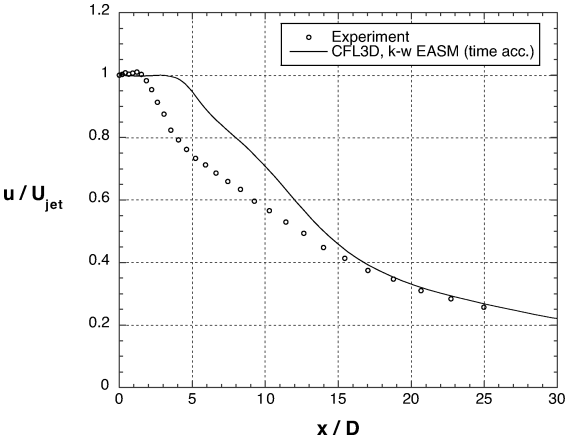

c) Explicit algebraic stress model

Fig. 4 Mean velocities along the centerline for the Mach 0.30 case using CFL3D and WIND.

that were used with both CFL3D and WIND (SA and SST), very similar predictions of axial-velocity decay were obtained. It can be observed that the SA results indicate closer agreement with the experimental data than the SST or Chien k–ϵ results. The two-equation models all demonstrated a significant delay in initial mixing rate relative to the experimental data. The minor differences in solutions between the Chien k–ϵ model and SST model (which effectively uses a k–ϵ model in the jet development region) are most likely caused by slight differences in the ϵ equation diffusion coefficient σ_ϵ used by the two models.

When attempting EASM calculations with both codes using the standard steady-state calculation procedure of employing a constant Courant–Friedrichs–Lewy (CFL) number but locally varying time step, only the k–ω EASM (using the new coefficients) resulted in a stable calculation, and even this calculation contained a large-scale unsteadiness in the initial part of the jet development region, which did not enable convergence to a steady flowfield solution. It is believed that the EASM calculations were unable to provide a converged solution for two reasons. First, the nearly incompressible Mach 0.30 nozzle flow exiting into quiescent air naturally leads to slow convergence for solvers such as CFL3D and WIND, which are designed for compressible flow simulations. The second, and likely more important, reason is that in examining Fig. 1 it can be observed that there is a very large base region (shown by the cross-hatching) surrounding the lobed nozzle exit, which leads to a highly separated flow, characterized by inherently large-scale unsteadiness surrounding the initial jet. The EASM formulations, unlike the linear one-equation or two-equation models, are sensitive to flow anisotropies caused by the large-scale unsteadiness present in the initial jet development region considered here. As a result, a time-accurate solution was pursued next. In Ref. 20, a time-accurate approach was required to obtain converged solutions for calculation of a multi-element airfoil exhibiting large-scale separation at high angles of attack. In Ref. 21, a highly overexpanded nozzle flow with a large separation also required a time-accurate solver to provide steady-state solutions. The time-accurate calculation used here with the EASM enabled a converged solution to be obtained, and the centerline velocities are shown in. Fig. 4c.

Comparisons of centerline turbulence intensities are provided in Fig. 5. Once again, solutions obtained with the SA and SST models are very similar when using CFL3D and WIND. The experimental data indicate two peaks of turbulence intensity. As indicated in Ref. 7, the first peak occurs when the shear layers from the lobes merge, while the second peak occurs after the outer shear layers

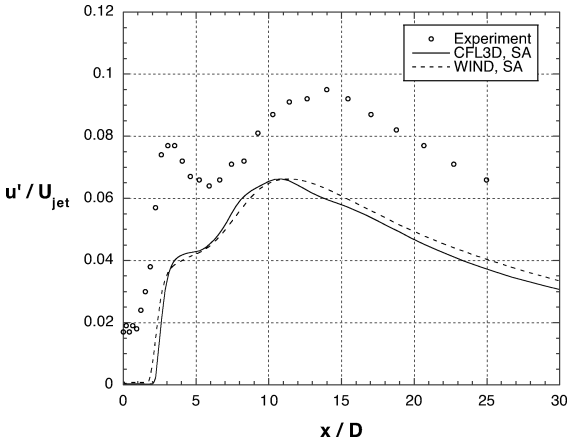

a) One-equation models

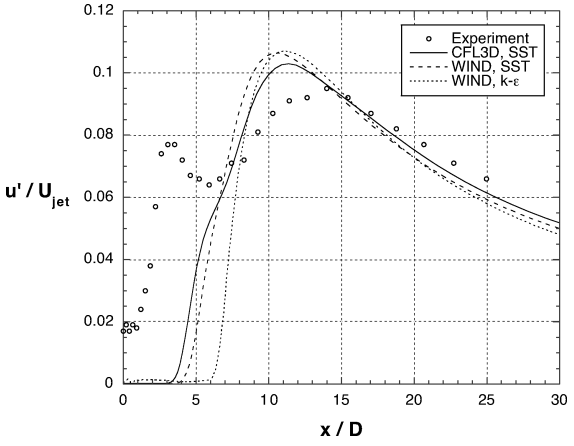

b) Two-equation models

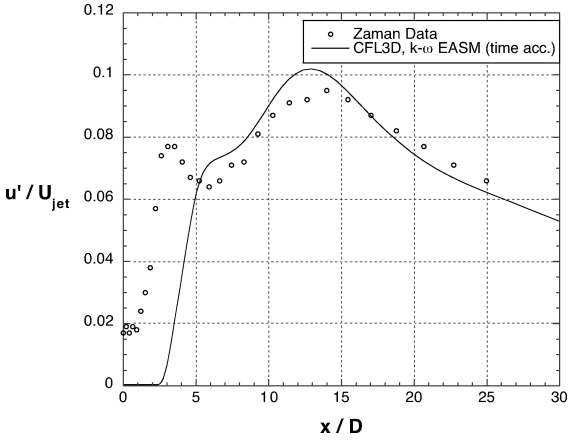

c) Explicit algebraic stress model

Fig. 5 Turbulence intensities along the centerline for the Mach 0.30 case using CFL3D and WIND.

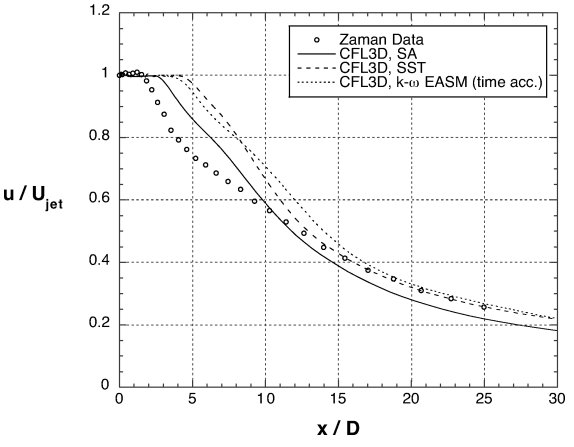

a) CFL3D

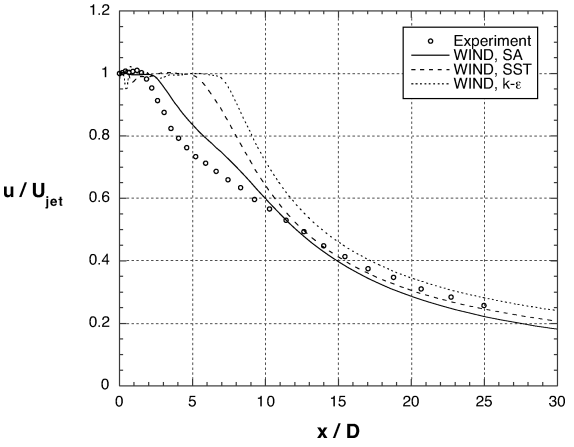

b) WIND

Fig. 6 Turbulence model effects on mean velocities along the centerline for the Mach 0.30 case.

merge at the jet centerline. None of the solutions obtained with any of the models are able to capture the first peak in as pronounced a manner as the experimental data. However, all of the models exhibit at least an inflection point in the turbulence intensity providing some evidence of shear-layer merging. The experiment indicates some turbulence at the jet centerline, even just downstream of the nozzle exit before any significant jet mixing occurs. It is hypothesized that a large fraction of what is experimentally measured as turbulence just downstream of the nozzle exit (near $x/D = 0.0$) along the centerline can be caused by fluctuations in the potential flow as a result of turbulence in the shear layer away from the centerline. The nature of the RANS calculations prohibits fluctuations in the inviscid core of the jet to be captured. Further, the turbulence models can only produce turbulence in the presence of mean velocity shear, which is absent here.

Comparisons of centerline velocities that highlight the effect of the turbulence models in CFL3D and WIND are shown in Figs. 6a and 6b, respectively. Parallel comparisons of centerline turbulence intensities are shown in Figs. 7a and 7b. In both codes, Fig. 6 indicates that the SA model provides the most rapid mixing and associated jet decay rate. Figure 7 shows substantial variations in the calculated centerline turbulence intensities, with only the k–ω EASM calculation providing close agreement to the experimental data.

Although the centerline profiles shown in Figs. 4–7 provide overall indications of the jet decay behavior, more details of the jet decay characteristics along the major and minor axes are shown for the mean axial velocities in Figs. 8 and 9. Detailed turbulence intensity profiles are shown in Figs. 10 and 11. In Fig. 8, it is observed that the SA calculation in both codes indicates the most rapid mixing of the individual lobe shear layers. The velocity profiles along the minor axis also show the most rapid mixing with the SA model, which is also in accordance with the previous centerline comparisons.

The turbulence intensity profiles show substantial variations depending on the turbulence model employed. Interestingly, at the two most downstream measurement stations, $x/D = 12.0$ and 18.0 in Figs. 10 and 11, the SA solution provides the worst agreement with the experimental data. This is because the SA model does not directly solve for the turbulent kinetic energy, unlike the other models employed in this study, and the derived turbulent kinetic energy is a function of the strain rate tensor as calculated by Eq. (10). The result of the SA approximation is that as the velocity profile becomes relatively flat the calculated turbulence intensity becomes too small. In considering only the mean axial-velocity predictions, it can be concluded that the SA model performed as well as any

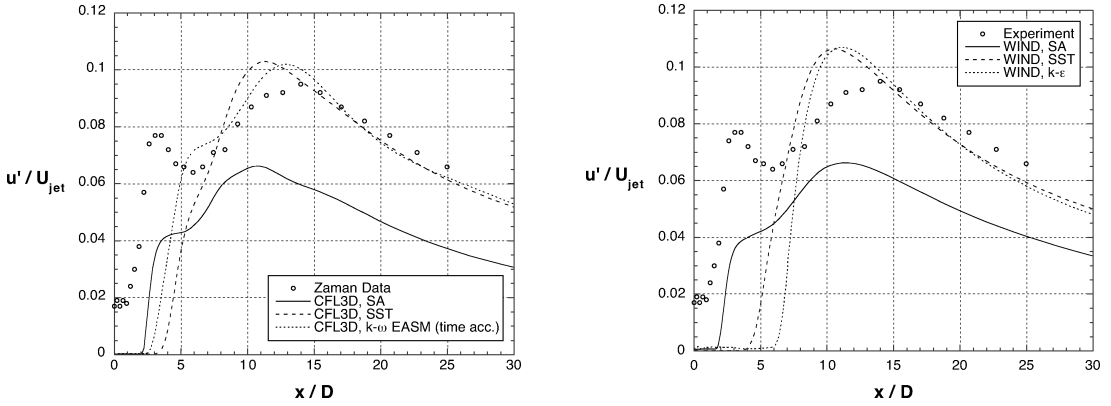

a) CFL3D b) WIND

Fig. 7 Turbulence model effects on turbulence intensities along the centerline for the Mach 0.30 case.

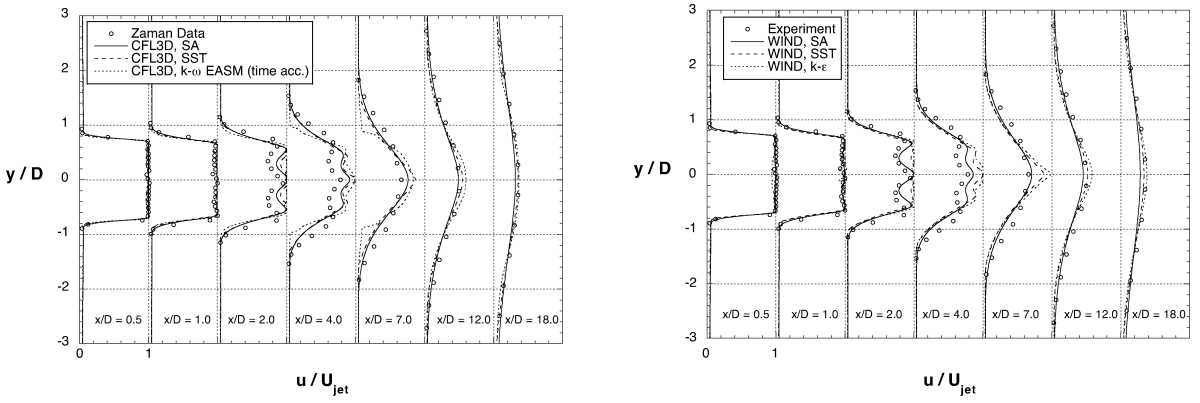

a) CFL3D b) WIND

Fig. 8 Turbulence model effects on mean velocity profiles along the major axis for the Mach 0.30 case.

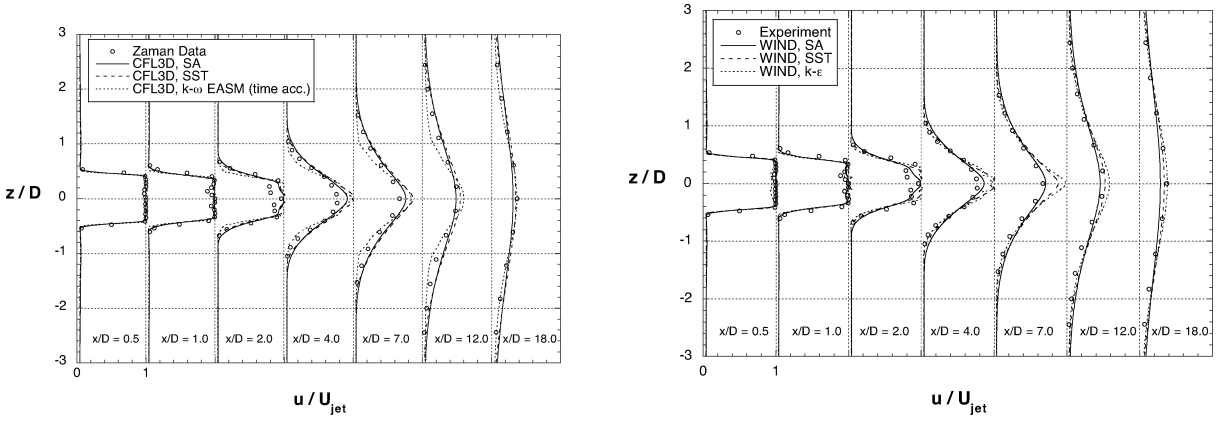

a) CFL3D b) WIND

Fig. 9 Turbulence model effects on mean velocity profiles along the minor axis for the Mach 0.30 case.

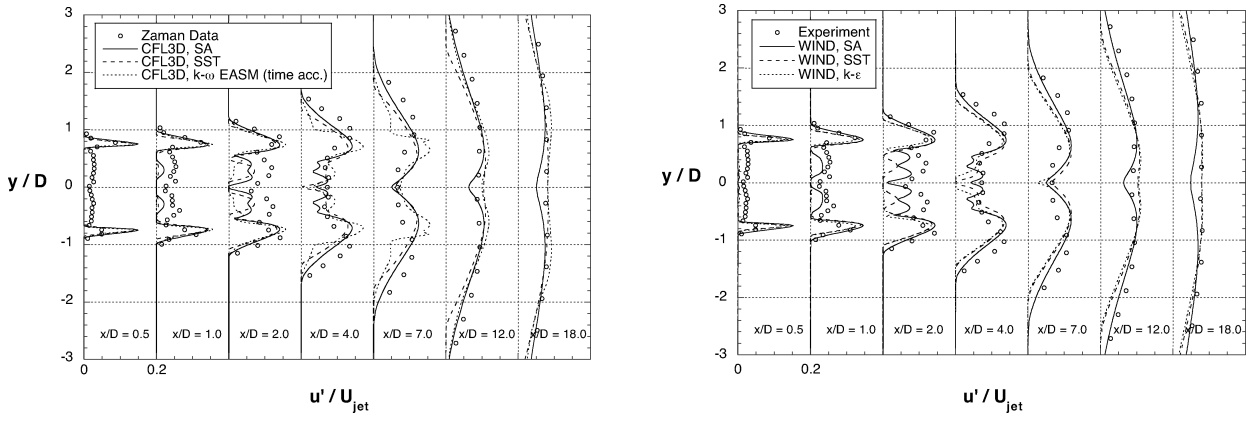

a) CFL3D b) WIND

Fig. 10 Turbulence model effects on turbulence intensity profiles along the major axis for the Mach 0.30 case.

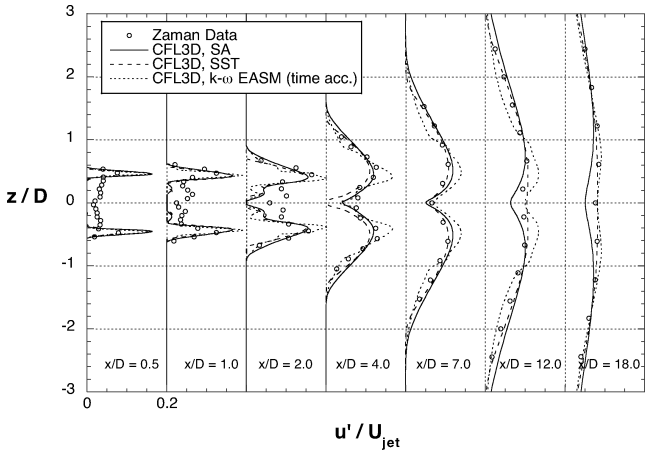

a) CFL3D

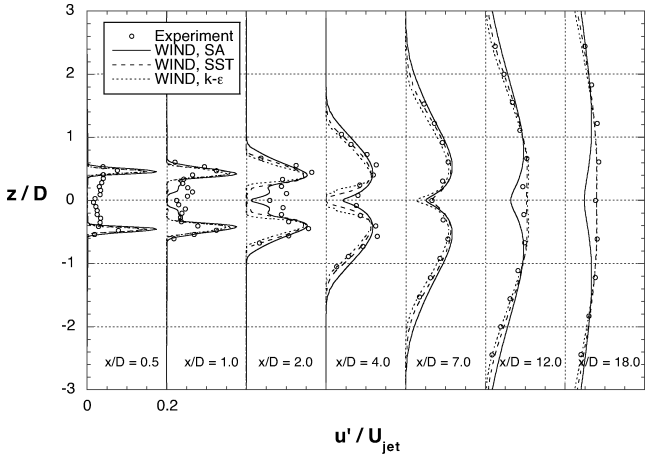

b) WIND

Fig. 11 Turbulence model effects on turbulence intensity profiles along the minor axis for the Mach 0.30 case.

of the models investigated here. However, the deficiency in the SA model far-field turbulence intensity would be undesirable if calculation of the turbulence intensity field is important, as in the case of a jet noise calculation employing the results of RANS flowfield computations.[22,23]

B. Mach 0.94 Nozzle Flow

As mentioned in the Introduction, limitations in using the hot-wire apparatus for extensive use in the high-speed flow of the Mach 0.94 case resulted in only centerline quantities being measured. Further, Ref. 7 indicates that the quantitative accuracy of the Mach 0.94 data is expected to be not as good as the Mach 0.30 data because the hot-wire measurements are approximations of mass flux ρu rather than velocity u alone, as described more completely in Refs. 7 and 24. For the Mach 0.30 case, the density is nearly constant throughout the flowfield. Although the Mach 0.94 case is not a highly compressible flow, the experimental quantities appearing in the subsequent mean velocity and turbulence intensity plots are actually $\overline{(\rho u)}/\overline{(\rho u)}_{\text{jet}}$ and $(\rho u)'_{\text{rms}}/\overline{(\rho u)}_{\text{jet}}$, respectively.

Comparisons of centerline axial velocities obtained within each class of turbulence model are presented in Fig. 12. Centerline turbulence intensities are provided in Fig. 13. As was the case for the Mach 0.30 results, the CFL3D and WIND implementations of the same models (SA and SST) produced very similar predictions. It can be observed that the SA results indicate closer agreement with the experimental data for the centerline velocities than the SST or Chien k–ϵ results. Unlike the Mach 0.30 results, the EASM calculations for Mach 0.94 displayed very little unsteadiness with the standard solution procedure employing a locally varying time step, yielding essentially converged steady-state solutions in both CFL3D

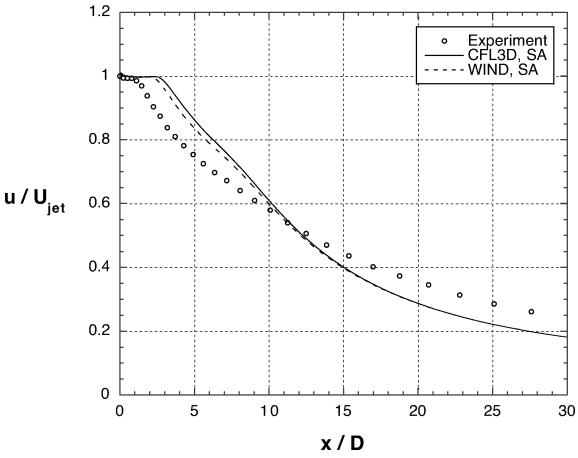

a) One-equation models

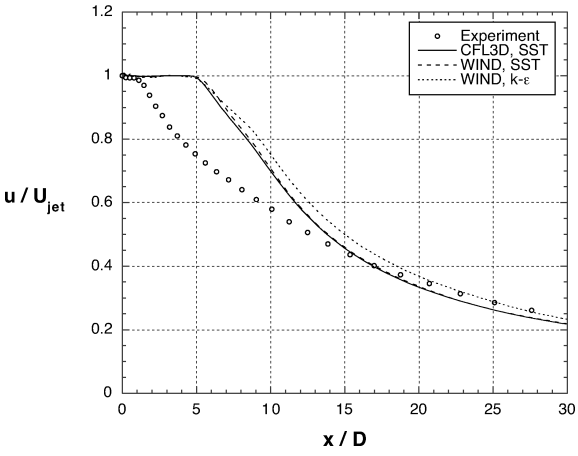

b) Two-equation models

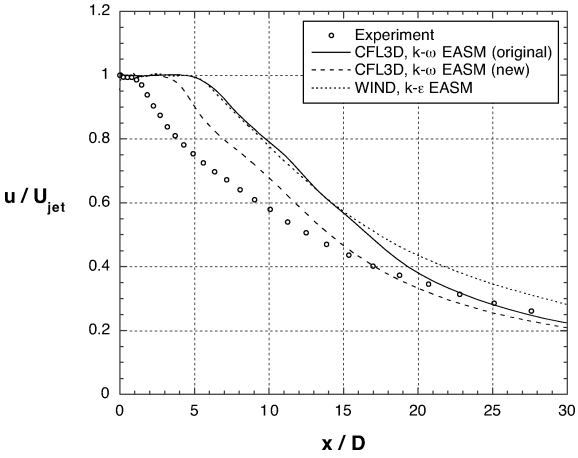

c) Explicit algebraic stress models

Fig. 12 Mean velocities along the centerline for the Mach 0.94 case using CFL3D and WIND.

and WIND. However, significantly more iterations were required to obtain solutions with the EASM approaches than with the linear models.

Two k–ω EASM solutions were obtained, the first using the original settings for σ_k and γ and the second using the new settings. As shown in Fig. 12c, the k–ω EASM solution using the new coefficients provided the highest level of mixing and closest agreement with experimental data. In Fig. 13, none of the solutions accurately capture the presence of the first turbulence intensity peak, but the k–ω EASM (new) solution indicates smaller discrepancies in prediction of the initial rise in turbulence intensity than the other two EASM solutions. Interestingly, the CFL3D k–ω EASM solution

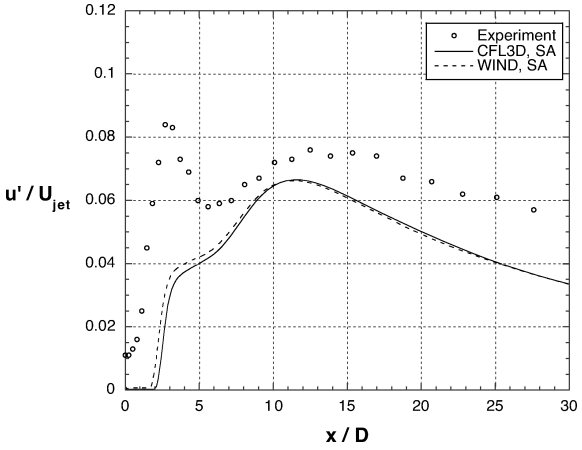

a) One-equation models

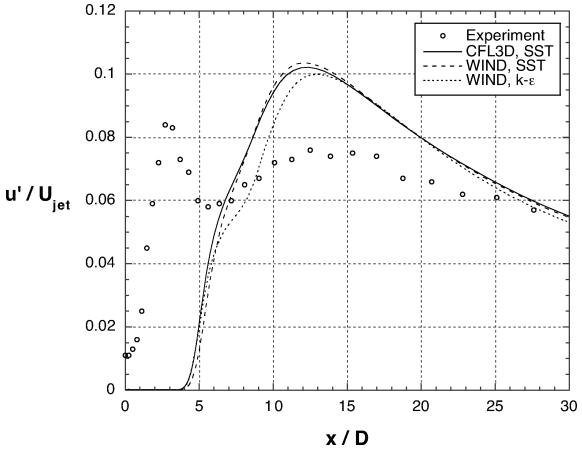

b) Two-equation models

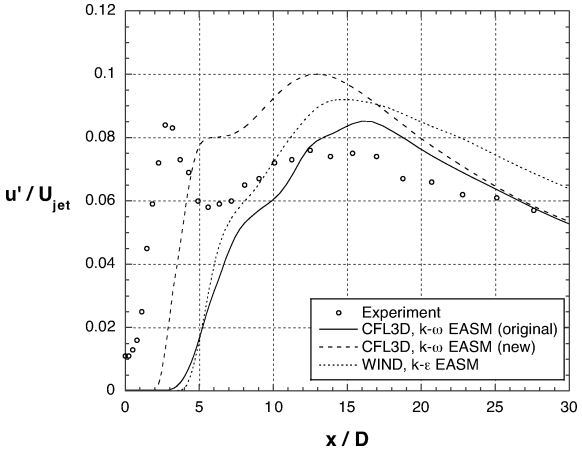

c) Explicit algebraic stress models

Fig. 13 Turbulence intensities along the centerline for the Mach 0.94 case using CFL3D and WIND.

with the original coefficient settings and the WIND k–ϵ EASM solution produce similar results.

The comparisons of centerline velocities using all of the turbulence models in CFL3D and WIND are shown in Figs. 14a and 14b. Comparisons of centerline turbulence intensities are shown in Figs. 15a and 15b. As was the case for the Mach 0.30 results, Fig. 14 indicates that the SA model provides the fastest jet decay rate. Figure 15 shows substantial variations in the calculated centerline turbulence intensities, with none of the solutions providing close agreement with the experimental data, although it is emphasized again that the Mach 0.94 experimental data were documented to have substantially more uncertainty than the Mach 0.30 data.

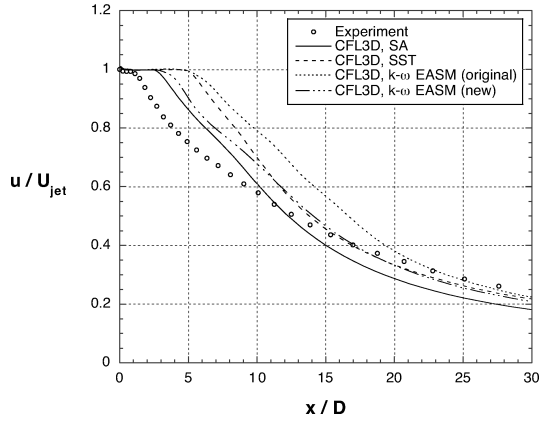

a) CFL3D

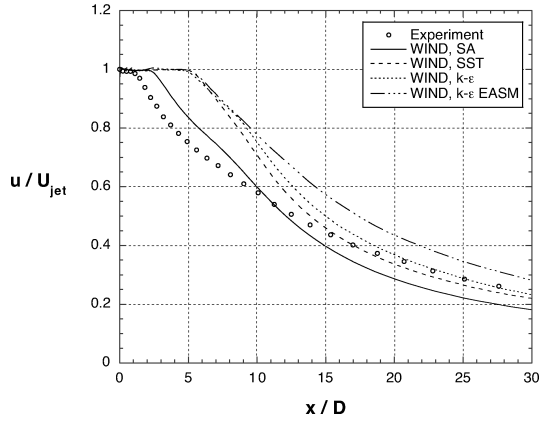

b) WIND

Fig. 14 Turbulence model effects on mean velocities along the centerline for the Mach 0.94 case.

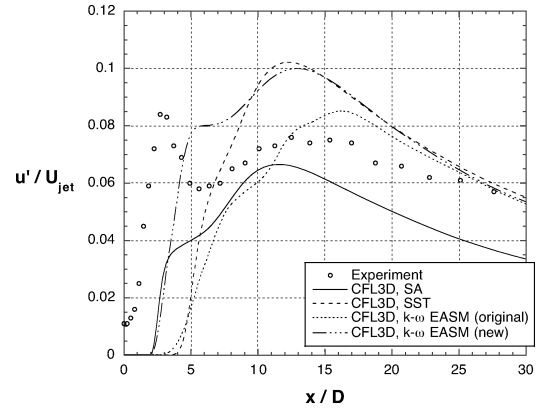

a) CFL3D

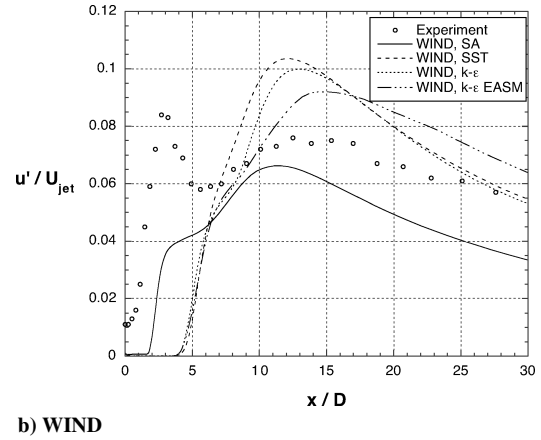

b) WIND

Fig. 15 Turbulence model effects on turbulence intensities along the centerline for the Mach 0.94 case.

V. Conclusions

The capabilities of several turbulence models in two general-purpose RANS solvers, CFL3D and WIND, were investigated for a highly three-dimensional flowfield originating from a six-lobed nozzle. Two nozzle operating points were considered, corresponding to Mach 0.30 and Mach 0.94 nozzle-exit conditions. Linear one-equation and two-equation models and nonlinear k–ω and k–ϵ EASM turbulence models were examined. Calculations obtained with the same linear eddy-viscosity models installed in the two codes yielded very similar results, whereas much more substantial differences were noted when varying the type of turbulence model within either single code. This indicates that the effects of turbulence modeling are significantly greater than any differences in code numerics between CFL3D and WIND.

Solutions obtained with the SA one-equation linear turbulence model generally indicated reasonable agreement with experimental data in terms of the mean axial-velocity predictions. Turbulence intensity predictions were in reasonable agreement with data in the near field of the jet but were not as good further downstream and were particularly deficient near the jet centerline. This is believed to be because of the approximation for turbulent kinetic energy, which is required with the SA model in order to derive the turbulent stress components. Calculations with the SST and Chien k–ϵ two-equation linear turbulence models resulted in significantly delayed initial mixing rates of the jet with surrounding ambient air, when comparing both the mean axial velocities and turbulence intensities with experimental data. Further downstream, the two-equation models yielded reasonable agreement with the data. None of the linear models was able to reproduce the experimental observation of two distinct turbulence intensity peaks along the jet centerline.

Two new coefficients for σ_k and γ in the k–ω EASM model were described in the context of the current jet flowfield. Although the changes were originally motivated by poor behavior for jet flow cases, these new coefficients are now also recommended in this model for general use as well. Specifically, for the Mach 0.94 case, results with the new coefficients resulted in improved mixing over results using the original coefficients. The k–ϵ EASM yielded delayed mixing similar to k–ω EASM results using the original coefficients.

For the Mach 0.30 case, the k–ϵ EASM was unable to run in a stable manner. The k–ω EASM calculation exhibited unsteady behavior and required a time-accurate calculation procedure to obtain a converged solution. This behavior was believed to be primarily caused by natural unsteadiness in the flowfield just downstream of the nozzle exit with large base region. The better convergence characteristics of the linear models are probably not an indication of higher accuracy of these simpler models, but instead they are able to more effectively smear the unsteadiness in the initial jet development region with their less sophisticated isotropic eddy-viscosity formulations.

The new k–ω EASM settings suggested in this paper for σ_k and γ indicate promise for flow problems dominated by turbulent mixing such as the nozzle flow considered here, and further investigations of these and other coefficients should be conducted for jet and similar mixing-dominated flows. There is room for significant improvement in capturing the delayed initial jet mixing rate. Previous to this work, most calibrations of the coefficients in the underlying two-equation models have been performed for wall-bounded turbulent flows.

Acknowledgments

This work was sponsored by the Propulsion and Power Program at NASA Glenn Research Center. David W. Lam and Mary Jo Long-Davis were project managers for this work.

References

[1]Barber, T. J., Chiappetta, L. M., DeBonis, J. R., Georgiadis, N. J., and Yoder, D. A., "An Assessment of Parameters Influencing the Prediction of Shear Layer Mixing," *Journal of Propulsion and Power*, Vol. 15, No. 1, 1999, pp. 45–53.

[2]Georgiadis, N. J., Yoder, D. A., and DeBonis, J. R., "A Comparison of Three Navier–Stokes Solvers for Exhaust Nozzle Flowfields," AIAA Paper 99-0748, Jan. 1999.

[3]Kenzakowski, D. C., "Turbulence Model Improvements for Jet Noise Prediction Using PIV Datasets," AIAA Paper 2004-2978, May 2004.

[4]Kenzakowski, D. C., and Papp, J. L., "EASM/J Extensions and Evaluation for Jet Noise Prediction," AIAA Paper 2005-0419, Jan. 2005.

[5]Ayyalasomayajoula, H., Kenzakowski, D. C., Papp, J. L., and Dash, S. M., "Assessment of k–ϵ/EASM Turbulence Model Upgrades for Analyzing High Speed Aeropropulsive Flows," AIAA Paper 2005-1101, Jan. 2005.

[6]Yoder, D. A., "Initial Evaluation of an Algebraic Reynolds Stress Model for Compressible Turbulent Shear Flows," AIAA Paper 2003-0548, Jan. 2003.

[7]Zaman, K. B. M. Q., Wang, F. Y., and Georgiadis, N. J., "Noise, Turbulence, and Thrust of Subsonic Free Jets from Lobed Nozzles," *AIAA Journal*, Vol. 41, No. 3, 2003, pp. 398–407.

[8]Barber, T. J., Chiappetta, L. M., and Zysman, S. H., "Assessment of Jet Noise Analysis Codes for Multistream Axisymmetric and Forced Mixer Nozzles," *Journal of Propulsion and Power*, Vol. 13, No. 6, 1997, pp. 737–744.

[9]Nelson, C. C., and Power, G. D., "CHSSI Project CFD-7: The NPARC Alliance Flow Simulation System," AIAA Paper 2001-0594, Jan. 2001.

[10]Krist, S. L., Bierdon, R. T., and Rumsey, C. L., "CFL3D User's Manual (ver. 5.0)," NASA TM-1998-208444, June 1998.

[11]Spalart, P. R., and Allmaras, S. R., "A One-Equation Turbulence Model for Aerodynamic Flows," *La Recherche Aerospatiale*, No. 1, 1994, pp. 5–21.

[12]Spalart, P. R., and Allmaras, S. R., "A One-Equation Turbulence Model for Aerodynamic Flows," AIAA Paper 92-0439, Jan. 1992.

[13]Chien, K.-Y., "Predictions of Channel and Boundary Layer Flows with a Low-Reynolds-Number Turbulence Model," *AIAA Journal*, Vol. 20, No. 1, 1982, pp. 33–38.

[14]Menter, F. R., "Two-Equation Eddy-Viscosity Turbulence Models for Engineering Applications," *AIAA Journal*, Vol. 32, No. 8, 1994, pp. 1598–1605.

[15]Menter, F. R., "Zonal Two Equation k–ω Turbulence Models for Aerodynamic Flows," AIAA Paper 93-2906, July 1993.

[16]Rumsey, C. L., Gatski, T. B., and Morrison, J. H., "Turbulence Model Predictions of Strongly Curved Flow in a U-Duct," *AIAA Journal*, Vol. 38, No. 8, 2000, pp. 1394–1402.

[17]Rumsey, C. L., and Gatski, T. B., "Recent Turbulence Model Advances Applied to Multielement Airfoil Computations," *Journal of Aircraft*, Vol. 38, No. 5, 2001, pp. 904–910.

[18]Rumsey, C. L., and Gatski, T. B., "Summary of EASM Turbulence Models in CFL3D with Validation Test Cases," NASA TM-2003-212431, June 2003.

[19]Georgiadis, N. J., Chitsomboon, T., and Zhu, J., "Modification of the Two-Equation Turbulence Model in NPARC to a Chien Low Reynolds Number k–ϵ Formulation," NASA TM 106710, Sept. 1994.

[20]Ying, S. X., Spaid, F. W., McGinley, C. B., and Rumsey, C. L., "Investigation of Confluent Boundary Layers in High-Lift Flows," *Journal of Aircraft*, Vol. 36, No. 3, 1999, pp. 550–562.

[21]DalBello, T., Georgiadis, N. J., Yoder, D. A., and Keith, T. G., "Computational Study of Axisymmetric Off-Design Nozzle Flows," AIAA Paper 2004-0530, Jan. 2004.

[22]Khavaran, A., and Georgiadis, N. J., "Aeroacoustics of Supersonic Elliptic Jets," AIAA Paper 96-0641, Jan. 1996.

[23]Khavaran, A., "Role of Anisotropy in Turbulent Mixing Noise," *AIAA Journal*, Vol. 37, No. 7, 1999, pp. 832–841.

[24]Zaman, K. B. M. Q., and Tam, C. K. W., "Flow and Noise Field of Subsonic Jets from Asymmetric Nozzles," AIAA Paper 99-3583, June 1999.